Journal of Structural Biology 183 (2013) 180–190

Contents lists available at SciVerse ScienceDirect

Journal of Structural Biology

journal homepage: www.elsevier.com/locate/yjsbi

Crystal lattice tilting in prismatic calcite

Ian C. Olson [a], Rebecca A. Metzler [b], Nobumichi Tamura [c], Martin Kunz [c], Christopher E. Killian [a], Pupa U.P.A. Gilbert [a,d,*]

[a] Department of Physics, University of Wisconsin–Madison, 1150 University Avenue, Madison, WI 53706, USA
[b] Department of Physics and Astronomy, Colgate University, Hamilton, NY 13346, USA
[c] Advanced Light Source, Lawrence Berkeley National Laboratory, 1 Cyclotron Road, Berkeley, CA 94720, USA
[d] Department of Chemistry, University of Wisconsin–Madison, 1101 University Avenue, Madison, WI 53706, USA

ARTICLE INFO

Article history:
Available online 24 June 2013

Keywords:
Biomineral
Mollusca
PIC-mapping
PEEM
Mesocrystal
Nanocrystal
Hardness

ABSTRACT

We analyzed the calcitic prismatic layers in *Atrina rigida* (*Ar*), *Haliotis iris* (*Hi*), *Haliotis laevigata* (*HL*), *Haliotis rufescens* (*Hrf*), *Mytilus californianus* (*Mc*), *Pinctada fucata* (*Pf*), *Pinctada margaritifera* (*Pm*) shells, and the aragonitic prismatic layer in the *Nautilus pompilius* (*Np*) shell. Dramatic structural differences were observed across species, with 100-μm wide single-crystalline prisms in *Hi*, *HL* and *Hrf*, 1-μm wide needle-shaped calcite prisms in *Mc*, 1-μm wide spherulitic aragonite prisms in *Np*, 20-μm wide single-crystalline calcite prisms in *Ar*, and 20-μm wide polycrystalline calcite prisms in *Pf* and *Pm*. The calcite prisms in *Pf* and *Pm* are subdivided into sub-prismatic domains of orientations, and within each of these domains the calcite crystal lattice tilts gradually over long distances, on the order of 100 μm, with an angle spread of crystal orientation of 10–20°. Furthermore, prisms in *Pf* and *Pm* are harder than in any other calcite prisms analyzed, their nanoparticles are smaller, and the angle spread is strongly correlated with hardness in all shells that form calcitic prismatic layers. One can hypothesize a causal relationship of these correlated parameters: greater angle spread may confer greater hardness and resistance to wear, thus providing *Pf* and *Pm* with a structural advantage in their environment. This is the first structure–property relationship thus far hypothesized in mollusk shell prisms.

1. Introduction

Mollusks are prolific, diverse, and sophisticated mineralizing organisms. They are widely distributed, and inhabit very different environments, thus they offer the possibility of correlating the shell structure with local environmental conditions (Lowenstam, 1954a,b; Olson and Gilbert, 2012; Olson et al., 2012) with the mechanical properties of the shells (Bruet et al., 2005; Kearney et al., 2006; Launey and Ritchie, 2009; Munch et al., 2008; Ritchie, 2011). The mollusks produce a huge variety of mineralized tissues that are presumably adapted to specific functions (Lowenstam and Weiner, 1989). Bøggild (1930) identified seven major types of shell structures, and these have been further sub-divided into 50 or so variants (Carter, 1980, 1990). The main structures are simple prismatic, composite prismatic, sheet nacre, columnar nacre, foliated, crossed-lamellar, and homogeneous structure (Taylor and Layman, 1972).

Both aragonite and calcite are found in mollusk shell structures, and, in different species, different structures are composed of one or both of these polymorphs (Lowenstam and Weiner, 1989; Mann, 2001). Here we study the prismatic layer of 8 nacre-forming mollusk shell species, all forming simple prismatic structures, made of calcite, except for *Nautilus*, in which the prismatic layer is made of aragonite spherulites.

The first discussion of mollusk prismatic layers appeared in 1844 (Carpenter, 1844). In all species, each prism is enveloped in an organic peri-prismatic sheath. Intra-prismatic proteins are also present (Aizenberg et al., 1994; Gotliv et al., 2005; Ndao et al., 2010; Politi et al., 2007). These organic peri- and intra-prismatic organic matrix molecules are formed first, and the minerals are assembled between or around the organic matrix. This matrix, therefore, must fulfill both a chemical and structural role, and is believed to mediate the mineral formation process. The precise mechanism of how organic molecules enact and control crystal nucleation, mineral polymorph selection, and crystallization kinetics is not known. However, recently the first complete mollusk genome was published (Zhang et al., 2012), and complete proteomes of different mollusk shell layers have been assembled (Marie

Abbreviations: *Ar*, *Atrina rigida*; *Hi*, *Haliotis iris*; *HL*, *Haliotis laevigata*; *Hrf*, *Haliotis rufescens*; *Mc*, *Mytilus californianus*; *Np*, *Nautilus pompilius*; *Pf*, *Pinctada fucata*; *Pm*, *Pinctada margaritifera*.

* Corresponding author at: Department of Chemistry, University of Wisconsin–Madison, 1101 University Avenue, Madison, WI 53706, USA. Mobile: +1 (608) 358 0164; fax: +1 (608) 265 2334.
E-mail address: pupa@physics.wisc.edu (P.U.P.A. Gilbert).

1047-8477/$ - see front matter © 2013 Elsevier Inc. All rights reserved.
http://dx.doi.org/10.1016/j.jsb.2013.06.006

et al., 2012). With the identification of the proteins associated with different structures of a mollusk shell, experimental determination of functions of specific proteins or protein complexes during shell formation will be feasible in the near future.

Furthermore, newly developed high-resolution methods have assisted the analyses of shell mineral structures and their orientations. These methods include Raman microscopy (Nehrke and Nouet, 2011), electron back scattered diffraction (Checa et al., 2009; MacDonald et al., 2010; Perez-Huerta et al., 2011), and polarization-dependent imaging contrast mapping (Gilbert, 2012; Gilbert et al., 2008, 2011; Killian et al., 2009, 2011; Ma et al., 2009; Metzler et al., 2007, 2008a). Some of these methods can also map minerals and organic components simultaneously (Gilbert et al., 2005; Metzler et al., 2010, 2008b; Nehrke and Nouet, 2011).

Suzuki and Uozumi (1981) observed optically that the surfaces of prisms, whether calcitic or aragonitic, are rather smooth and structureless. However, observation with an electron microscope reveals that the prisms are built up of very small calcium carbonate crystals (Suzuki and Uozumi, 1981), as was previously observed by Watabe and Wada (1956), Tsujii et al. (1958), Taylor and Layman (1972), Nakahara and Bevelander (1971).

The subdivision of molluscan calcite prisms into 50–100 nm nanoparticles is a well-established observation (Bruet et al., 2005; Dauphin, 2001, 2008; Li et al., 2004; Wolf et al., 2012). Many authors had assumed that organics separate these nanoparticles (Rousseau et al., 2005; Wolf et al., 2012), however, the Estroff group showed with electron tomography that organic molecules within the calcite prisms of *Atrina rigida* are instead concentrated in sparse, disk-like nanopatches that are not connected (Li et al., 2011).

For this work we selected 8 mollusk shell species to observe structural differences for the different prismatic layers and attempt to correlate the observations with mechanical properties. All of the selected shells are also nacre-forming, but this is not directly relevant to this work. Seven of them have calcite prisms (*Ar*, *Hi*, *HL*, *Hrf*, *Mc*, *Pf*, *Pm*) and one has aragonite spherulites (*Np*) in their prismatic layers. These shells are representative of 3 classes of shell-forming mollusks: 4 are bivalves (*Ar*, *Mc*, *Pf*, *Pm*), 3 are gastropods (*Hi*, *HL*, *Hrf*), and 1 is a cephalopod (*Np*).

The structure, microstructure and crystallography of calcite and aragonite prisms here were analyzed with various high-resolution methods, in order to compare quantitative results with hardness values. These experiments are designed to reveal structure–property relationships, which, thus far, have been the subject of few studies in mollusk prisms.

2. Materials and methods

2.1. Samples

We analyzed a total of 13 shells from 8 different molluscan species, described here. *Haliotis laevigata* (*HL*): The *HL* 1 specimen, 156 mm length, was collected in Western Australia and purchased from Australian Seashells PTY Ltd (Kingsley, Australia); the *HL* 2 specimen, 148 mm length, was provided by Prof. Monika Fritz and originally purchased from Australian Abalone Exports PTY Ltd (Victoria, Australia). *Haliotis iris* (*Hi*): The *Hi* specimen, 107 mm length, was collected in New Zealand and purchased from Australian Seashells PTY Ltd (Kingsley, Australia). *Haliotis rufescens* (*Hrf*): The *Hrf* specimen, 78 mm length, was farm-raised in Santa Cruz, CA and purchased from the Tokyo Fish Market in Berkeley, CA. *Mytilus californianus* (*Mc*): The *Mc* specimen, 148 mm length, was collected from the wild in Bolinas, CA. *Nautilus pompilius* (*Np*): The *Np* 1 specimen, 183 mm length, was collected offshore Siquijor Island, Philippines and purchased from Conchology, Inc., Philippines; the *Np* 2 specimen, 142 mm length, was collected offshore Jolo Island, Philippines and purchased from Conchology, Inc., Philippines. *Atrina rigida* (*Ar*): The *Ar* 1 specimen, 161 mm length, was collected from Belleair Beach, Florida and purchased from the collection of Robert Marchiselli; the *Ar* 2 specimen, 165 mm length, was collected at low tide on Sanibel Island, Florida. *Pinctada fucata* (*Pf*): The *Pf* 1 specimen, 58 mm length, was purchased from Hai de Ming Pearl Co. Ltd. Liusha Town, Zhanjang, China; the *Pf* 2 specimen, 58 mm length, was purchased from Hai de Ming Pearl Co. Ltd. Liusha Town, Zhanjang, China. *Pinctada margaritifera* (*Pm*): The *Pm* 1 specimen, 99 mm length, was farm-raised in the inner lagoon of the Rangiroa atoll, French Polynesia and purchased from the Gauguin Pearl Farm; the *Pm* 2 specimen, 90 mm length, was farm-raised in the inner lagoon of the Rangiroa atoll, French Polynesia and purchased from the Gauguin Pearl Farm.

With one exception, all samples were cut with a jeweler's saw, embedded in epoxy (EpoFix, Electron Microscopy Sciences, PA), and polished with decreasing size alumina grit down to 50 nm (MasterPrep, Buehler, IL). This exposed the shell cross-sections as imaged in the visible light micrographs.

The *Np* 2 sample was cut with a jeweler's saw, and tripod-polished at an angle of 2° using diamond grinding discs, so the sample was wedge-shaped with a final maximum thickness <100 μm. After tripod-polishing the thin wedge sample was mounted on a washer for analysis.

2.2. VLM with crossed polarizers

Visible light microscopy (VLM) images were obtained using a Zeiss Axio Imager.A1m microscope that works in reflected light, with a mounted Jenoptik ProgRes C12plus camera. The illumination channel is equipped with a fixed linear polarizer, whereas the analysis channel has a rotating linear polarizer, with quantitative and accurate angle positioning and measurement. Birefringent samples, such as calcite and aragonite in the mollusk shells imaged here, generate crystal-orientation-dependent contrast when illuminated with polarized light. The angle of the analysis polarizer was selected to maximize contrast in the VLM images and was always around 90°, hence all images are acquired with crossed-polarizers. Partly overlapping VLM images were stitched and blended in Adobe Photoshop using the Auto-Blend Layers tool, and the color levels were also enhanced for display.

2.3. Microdiffraction

Synchrotron Laue micro-X-ray diffraction experiments were performed on beamline 12.3.2, at the Advanced Light Source at Lawrence Berkeley National Laboratory in Berkeley, CA. The instrument uses Kirkpatrick-Baez mirror optics to focus the X-ray beam down to a size of about $1 \times 1\ \mu m^2$ in cross-section at the sample position. The samples were mounted on a precision XY stage and illuminated with white beam X-ray radiation ($5\ keV < E < 22\ keV$, pink beam). Various sample geometries were used, as described below. In all cases, X-ray microdiffraction patterns were obtained using a Pilatus 1 M X-ray detector. The area detector was at a distance of ~140 mm from the sample. The exact detector position and sample orientations were calibrated using the Laue diffraction pattern of a silicon crystal. With the following exceptions, diffraction maps were 500 μm in horizontal, along the nacre-prismatic-boundary, and 200 μm in vertical, with a 5 μm step size. The *Np* 2 map was 100×100 μm with a 1 μm step size, the *Hrf* map was 300×300 μm with a 5 μm step size, and the *Pm* 2 map was 200×200 μm with a 5 μm step size. The *Np* 2 map was taken in transmission geometry with a 90° incident angle, and detector angle of $2\theta = 60°$, the *Hrf* and *Pm* 2 maps were taken in reflection geometry with a 25° glancing incidence angle and detector angle

of $2\theta = 70°$. All other maps were acquired in reflection geometry with an incidence angle of 45° and a detector angle of $2\theta = 90°$. The exposure time for each diffraction pattern was 1 s (*Np* 2, *Hrf*, *Pm* 2) or 2 s (all other samples). Each Laue X-ray microdiffraction pattern was indexed using the XMAS (X-ray Microdiffraction Analysis) software (Tamura et al., 2003). Indexing provides the full 3-dimensional orientation matrix for each crystal, making it possible to map the orientations of aragonite or calcite crystallites in the sample. Analysis was performed on a 48 node Linux cluster which enables the automated processing of thousands of Laue microdiffraction patterns to map the distribution of the orientation of all calcium carbonate crystals in the sample. Measurements of angle spread were made based on the distribution of reflections present in a pole-figure for each diffraction map.

2.4. PIC-mapping

PIC-mapping experiments (Gilbert, 2012; Gilbert et al., 2011; Metzler et al., 2007, 2008a; Olson et al., 2012) were performed with the PhotoEmission Electron Microscope (PEEM) (De Stasio et al., 1992a,b; De Stasio et al., 1993a,b; De Stasio et al., 2003; Gilbert et al., 2003) PEEM-3 on beamline 11.0.1 at the Advanced Light Source at Lawrence Berkeley National Laboratory in Berkeley, CA. The beamline is equipped with a state-of-the-art elliptically polarizing undulator (EPU) providing precise selection of X-ray energy and linear X-ray polarization. The microscope was operated in a mode capturing 1030×1054 pixel images of a 20 μm field of view, with ~20 nm pixel dimensions. PIC-mapping is sensitive to the 2-dimensional projection (c'-axis) of calcite and aragonite *c*-axis orientation (Gilbert, 2012; Gilbert et al., 2011)), and can resolve crystal orientations within 2° (Olson et al., 2013a,b).

2.5. Microindentation

Microindentation is used to probe the hardness of a variety of materials, including biominerals, on a micron scale, enabling the correlation of hardness with local properties (Moureaux et al., 2010; Schmahl et al., 2008; Wang et al., 1997). The microindentation experiments reported here were conducted on shells and $CaCO_3$ crystals, using a Pace Technologies HV-1000Z micro-hardness tester equipped with a Vickers, square pyramidal, indenter tip (http://www.metallographic.com). For each indent, a load of 98 mN was applied to the surface of the sample for a period of 15 s. The hardness at the location of the indent was determined by measuring the diagonals of the resulting indent, with larger diagonals indicating a smaller hardness value (HV), as described by the equation:

$$HV = F/A \approx 0.1891F/d^2$$

where the force (F) is measured in Newtons and the diagonals (d) are measured in millimeters (http://www.gordonengland.co.uk/hardness/microhardness.htm). The diagonals of the indents were measured by VLM with a 50× objective lens and with a scanning electron microscope (SEM) (JEOL JSM636OLV SEM at Colgate University, Hamilton, New York), in the secondary electron imaging mode, at 3500×. The higher-magnification SEM imaging provided greater precision, thereby reducing the standard deviation of the measurements, but all data from VLM and SEM micrographs are usually consistent, unless otherwise described below.

A total of 20–70 indents were done for each sample. Indents that fell on prism-prism boundaries or on organic envelopes, indents that resulted in shattering or significant surface deformation, and indents imaged with SEM that could not be accurately measured were excluded. The 20–70 indents were made on many different prisms with greatly varying crystal orientations, as shown in Fig. 8, to average out orientation effects. The biomineral samples used for the microindentation experiments were the same as used for microdiffraction and PIC-mapping experiments; the only difference is that the platinum coating was removed by polishing with 50 nm alumina grit before microindentation. For the *Haliotis rufescens* (*Hrf*) and *Pinctada fucata* (*Pf*) samples, measurements were done before and after soaking the samples in artificial seawater for 24 h. There was no significant difference in the hardness (measured from SEM micrographs) between dry and wet shells for *Pf* (dry 278, wet 268), with a p-value of 0.1, though we found a significant difference in the hardness for *Hrf* (dry 255, wet 228), with a p-value of 6×10^{-5}. Using the VLM micrographs to measure indent diagonals, instead, we found that in both cases dry and wet sample were not significantly different, *Pf* hardness (dry 284, wet 270) with a p-value of 0.1, and *Hrf* hardness (dry 260, wet 272) with a p-value of 0.2. Based on these results, all other hardness measurements in this work were done with dry samples.

The geologic aragonite sample consisted of several small (1–5 mm) research grade aragonite crystals, purchased from Ward Scientific and originating from Minglanilla, Cuenca, Spain. They were embedded in epoxy and polished with decreasing alumina grit down to 50 nm; indents were collected on 3 geologic aragonite crystals of random orientation to remove orientation effects. The synthetic calcite crystals were grown on a glass slide in a solution containing $CaCl_2$, in the presence of NH_4CO_3 vapor; after growth, the crystals were 50–100 μm in size. They were rinsed in ethanol, dried, then embedded in epoxy and polished, as described above. Randomly oriented crystals were exposed at the surface of the polished sample, thus each indentation was done on a different, randomly oriented synthetic calcite crystal, once again to remove orientation effects. Two geologic calcite crystals were analyzed at two orientations. The first sample was a ~5 mm crystal with (100) orientation (MTI Corporation, Richmond, CA, USA), embedded, and polished, as described above. The second sample was oriented so indents were done on a (104) calcite cleavage plane, part of a ~11 mm research grade calcite crystal purchased from Ward Scientific, and originating from Chihuahua, Mexico. HV results from the two geologic calcite crystals were averaged together to eliminate orientation effects. All HV data from SEM and VLM, raw and averaged, are presented as supporting information in an Excel file.

2.6. Correlation

The correlation of HV and angle spread (AS) was obtained in Kaleidagraph® 4.1.3 for Macintosh. We first plotted all HV and AS values, including measurements in duplicate shells, we then did a linear fit of the data, and obtained the linear equation in Fig. 7: $HV = 257 + 1.3\ AS$, with correlation coefficient $R = 0.86$ and $R^2 = 0.74$.

2.7. Reflection width

We measured the width of individual diffraction reflections on the 2D detector, and then calibrated the spatial width for each acquisition considering the detector angle with respect to the X-ray beam and its distance from the diffracting sample, thus converting the width into an angular width. The intensity profile of each reflection spot was first fitted to a Gaussian, then the full width at half maximum (FWHM) of this Gaussian was measured and chosen to represent the reflection width in degrees. Each measurement was repeated 10 times, representing a variety of reflections and diffraction patterns from each species. The plot of HV vs reflection FWHM was also fit to an exponential curve to guide the eye, but this fit should not be considered quantitative, as one cannot assume a straightforward relationship between

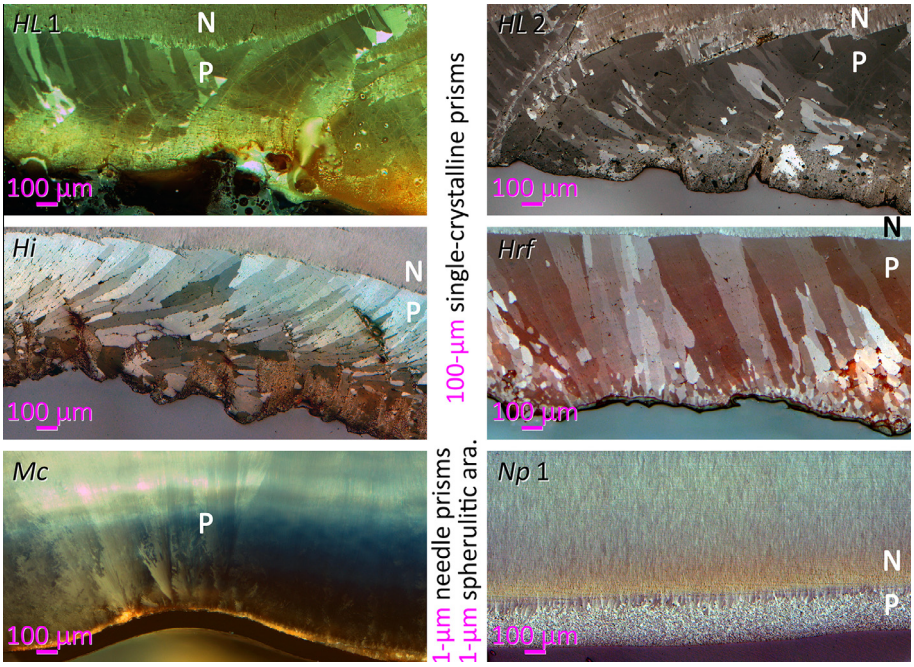

Fig.1. Visible light micrographs (VLM) obtained in reflected light, with crossed-polarizers, from polished cross-sections of six shells. In all shells the nacre layer (N) and the prismatic layer (P) are at the top and bottom, respectively. Notice in the *Haliotis* shells, the contrast across 100-µm wide prisms, which appear with different brightness depending on their *c*-axis orientation. Bundles of fine, apparently co-oriented calcite needles, ~1-µm wide, are observed in *Mc*, while in *Np* the prismatic layer is entirely composed of spherulitic aragonite, with each crystal ~1-µm wide. High-resolution versions of these images are available online as a tif file.

particle size and reflection width in the case of Laue diffraction. The width of each reflection is indeed affected by both the particle size and the angle spread of particle orientations along the beam path, and to calculate FWHM, care must be taken to select the reflection direction for which the orientation effect is minimized, that is, the direction perpendicular to the smear direction. The only certain statement is that the greater the FWHM the smaller the particle size, and the greater their AS.

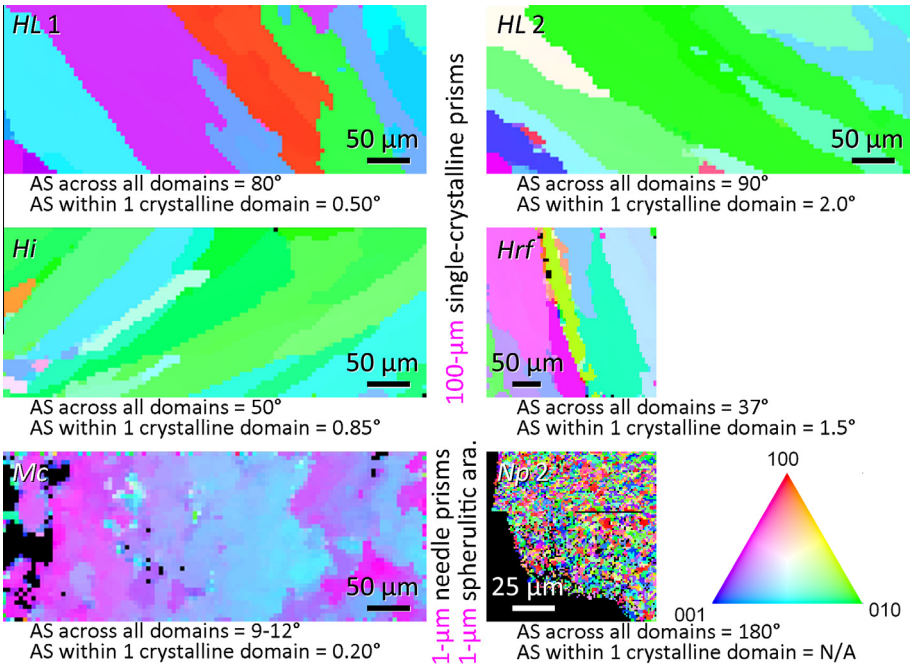

Fig.2. Microdiffraction maps of the same shells in Fig. 1, but imaged at much greater magnification, and analyzed with Laue diffraction only in the prismatic layer regions, away from the nacre-prismatic boundary. Colors indicate the orientation of the calcite or aragonite crystals. The triangle at the bottom right provides a visualization of the color scheme. If a pixel appears red, green or blue, the *a*-, *b*-, or *c*-axis of the crystal in that position is perpendicular to the plane of the image. Because each of the 100-µm prisms in *Haliotis* displays a single color, we can conclude that it is a single-crystalline prism, with internal angle spread (AS) varying between 0.2° and 2°, depending on the species. In other words, a crystalline domain, in *HL*, *Hi*, *Hrf*, *Mc*, and *Np* is a single prism. Angle spreads across all calcite prisms in these shells vary between 9° and 90°. Different calcite needles in *Mc* are not as co-oriented as they appear in VLM (Fig. 1), but coarsely co-oriented within 12°. The aragonite spherulites in *Np* are randomly oriented with respect to one another (AS = 180°).

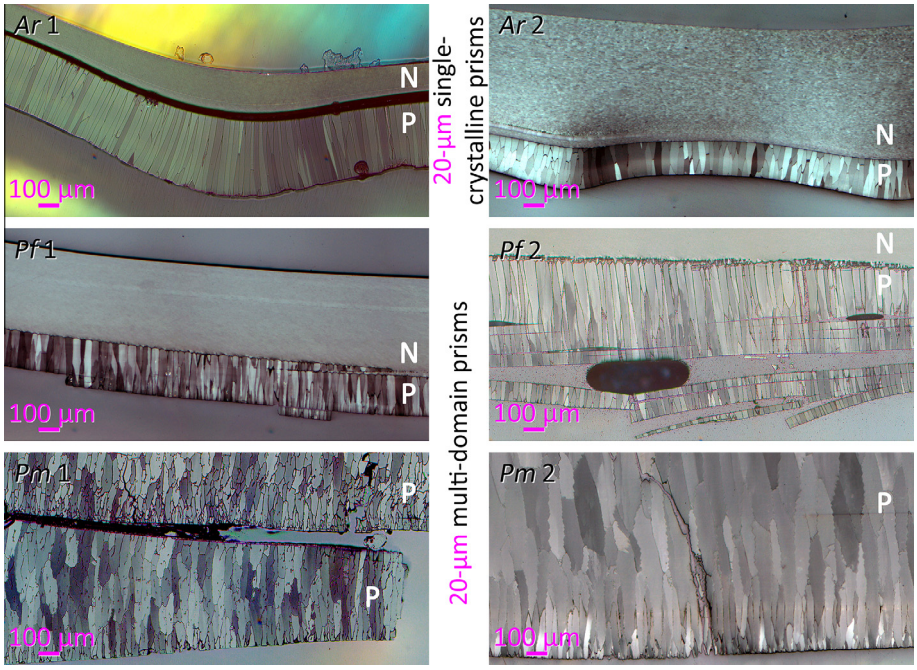

Fig.3. VLM, crossed-polarizer micrographs of 6 more shells from 3 species. Again N and P label nacre and prismatic layers, respectively. At this magnification *Ar*, *Pf* and *Pm* all show 20-µm wide calcite prisms. The most striking difference is that the *Pinctada* species exhibit lamellae departing from the main prismatic layer, whereas *Atrina* has a compact prismatic layer. The dark spot in sample *Pf* 2 is an air bubble not filled by epoxy, trapped between two prismatic lamellae. High-resolution versions of these images are available online as a tif file.

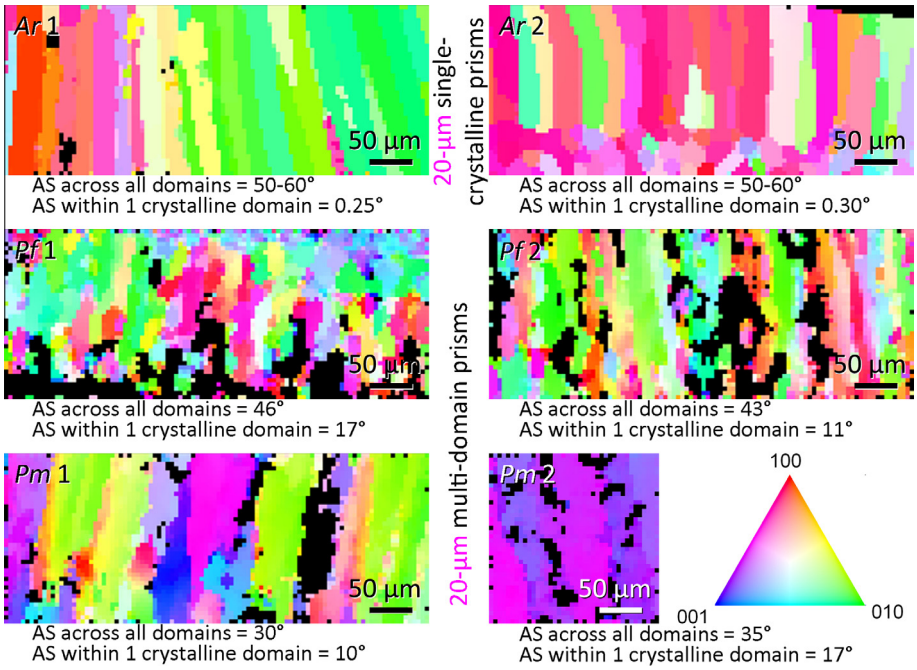

Fig.4. Microdiffraction maps of the same shells in Fig. 3, again imaged at much greater magnification using the same color scheme as in Fig. 2. As in *Haliotis*, the *Atrina* prisms are composed of a single crystalline domain with angle spread smaller than 0.3°, and at ~20-µm wide are much smaller than prisms in Haliotis (Fig. 2). In Fig. 3 *Atrina* and *Pinctada* prisms appeared similar in shape, size and contrast. Here microdiffraction clearly shows that the *Pinctada* species (*Pf* and *Pm*) do not have single-crystalline but multi-crystalline-domain prisms, as shown by gradients of color in each polychromatic prism. The angle spread within one crystalline domain in Pf and *Pm* is on the order of 10°-20°.

3. Results

Here we analyzed 13 shells representing 8 different mollusk species, and found that they are quite diverse, as presented in Figs. 1–4. Specifically, the various shells exhibit either:

- 100-µm wide single-crystalline calcite prisms (*HL*, *Hi*, *Hrf*).
- 1-µm wide needle-shaped calcite prisms (*Mc*).
- 1-µm wide spherulitic aragonite (*Np*).
- 20-µm wide single-crystalline calcite prisms (*Ar*).
- 20-µm wide multi-domain calcite prisms (*Pf*, *Pm*).

In Figs. 1 and 3 we show visible light micrographs (VLM) of 12 shells, and in Figs. 2 and 4 microdiffraction maps of the same

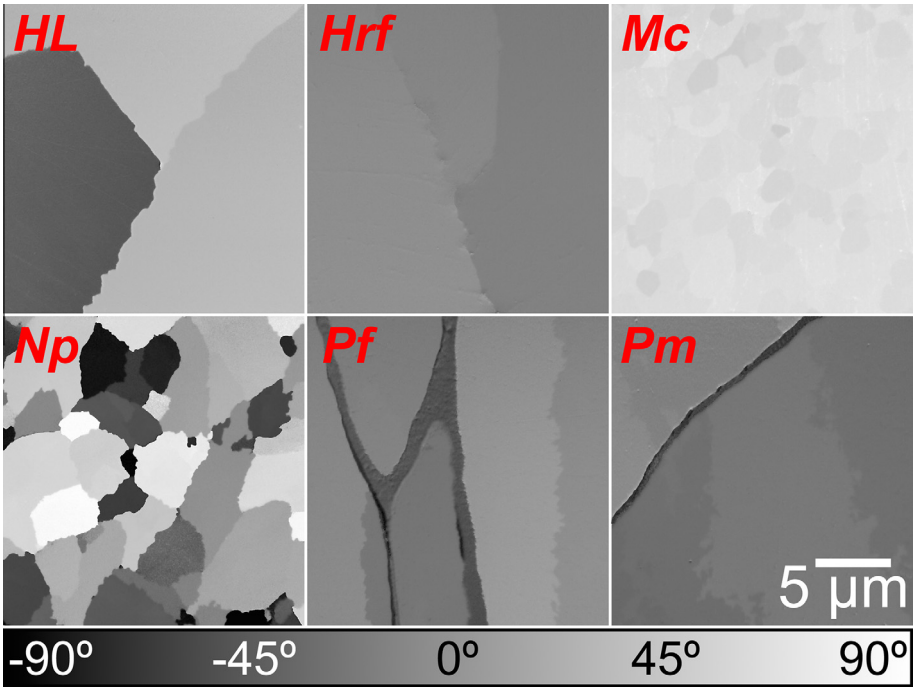

Fig.5. PIC-maps of 20 × 20 μm portions of the prismatic layer in 6 of the 8 mollusk shell species studied here. In a PIC-map the gray level represents the orientation of the *c*′-axis (Gilbert, 2012; Gilbert et al., 2011; Olson et al., 2012). Here all PIC-maps are displayed with the same gray scale, as indicated at the bottom, hence the presence of black and white in *Np* confirms that the aragonite spherulites are randomly oriented, whereas the small contrast observed in *Mc* confirms that the needles are co-oriented within 12°. The *Mc* needles are imaged in cross-section here, thus they appear as spherulites. *HL* and *Hrf* show larger, singly oriented prisms as expected. Interestingly, *Pf* and *Pm* show well-distinct sub-prismatic domains with different calcite crystal orientations. These domains have jagged but sharp edges, demonstrating that each prism is composed of a myriad of nanoparticles 50–100 nm in size, as previously observed (Bruet et al., 2005; Dauphin, 2001, 2008; Gilbert et al., 2011; Li et al., 2004; Nakahara and Bevelander, 1971; Suzuki and Uozumi, 1981; Taylor and Layman, 1972; Tsujii et al., 1958; Watabe and Wada, 1956; Wolf et al., 2012), and each prism contains several of these discrete, sharply delimited domains. Similar jagged, sharp domain edges are apparent in the PIC-maps from *HL*, *Hrf*, and *Np*. The thick organic periprismatic sheaths appear as dark stripes in *Pf* and *Pm* PIC-maps. They show that in *Pf* we are looking at small portions of four different prisms, and in *Pm* we see small portions of two prisms. Notice that while the same crystal orientation propagates through an organic envelope occasionally, most often it does not. High-resolution versions of these images are available online as a tif file.

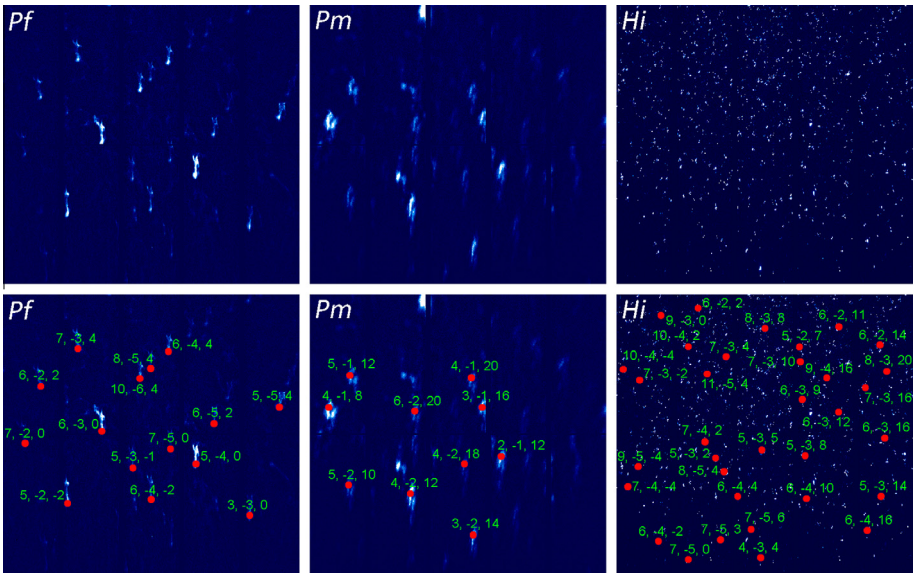

Fig.6. Laue diffraction patterns obtained by illuminating with X-rays a 1 μm^2 spot, 100-μm deep volume of the prismatic layer of *Pf*, *Pm*, and *Hi* shells. Notice the sharp, single-dot reflections in *Hi*, and the elongated diffraction "smears" in *Pf* and *Pm*, generated by crystal lattice tilting and its angle spread within sub-prismatic domains. The bottom three images are repeats of the above images, in which the brightest spots or smears have been indexed.

shells, but at higher magnification. In VLM images the contrast of brightness is due to differences in *c*-axis orientation, whereas in microdiffraction maps the color indicates quantitatively the orientation of the crystal in each pixel. The results obtained from the two methods in Figs. 1 and 2 are in excellent agreement, as are those in Figs. 3 and 4. These data highlight the different prismatic

structures listed above. It is intriguing that the prisms in the *Pinctada* species *Pf* and *Pm* are not single- but poly-crystalline. Multi-domain prisms appear as having different gray levels within a single prism in the VLM images in Fig. 3, in the high-resolution version of the same figure provided online, and are quite clear in the polychromatic diffraction maps of Fig. 4.

The observation in Fig. 4 that *Pf* and *Pm* have multi-domain prisms piqued our interest. We therefore further analyzed the prismatic layers of many of these shells with PIC-mapping, to see with higher-resolution how the different orientations are distributed in space, within each prism. In Fig. 5 we present the PIC-mapping results, which are in good agreement with microdiffraction.

In the microdiffraction maps in Fig. 4 there is evidence of crystal lattice tilting within each prism. The tilting appears as a gradient of color, in most prisms of *Pf* and *Pm*, whereas the PIC-maps of Fig. 5 and others show very few (3 in Fig. 5, up to 6 in other data not shown), discrete, abruptly changing orientations in each prism. How do we reconcile these data? We propose that the correct answer is provided by microdiffraction, and the apparent discrepancy can be understood considering the sampling difference between PIC-mapping and microdiffraction. The PIC-maps are small, only 20 μm × 20 μm × 3 nm thick. Whereas the microdiffraction maps are large, 500 × 200 × 100 μm thick. For PIC-mapping the thickness is the escape depth of the detected photoelectrons, which is on the order of 3 nm (Frazer et al., 2003; Gilbert et al., 2005). For diffraction maps the thickness is the penetration depth of the X-ray beam in calcite (~200 μm) (CXRO) and the escape depth of the reflected X-rays that reach the detector (~100 μm). PIC-mapping is insensitive to crystal lattice tilting that occurs at the 100-μm scale, because it samples too small a volume in a large sample with a slowly-tilting crystal lattice. The observation of crystal lattice tilting is worth further investigation, as it may shed some light on how prisms form: do they really have amorphous precursors as several authors have proposed (Baronnet et al., 2008; Dauphin, 2008; Jacob et al., 2011; Kim et al., 2011b, 2011a; Nudelman et al., 2007)? Do they aggregate first, and then crystallize (Wolf et al., 2012)? Or could they form by oriented attachment (Penn and Banfield, 1998b,a)?

In Fig. 6 we present Laue diffraction figures acquired from 3 different shells, the two *Pinctada* species, *Pf* and *Pm*, and one *Haliotis* species, *Hi*. Notice that each of these were acquired from a single micro-beam position on the shell, hence they are identical to those obtained and then analyzed for each single pixel in the maps of Figs. 2 and 4. The beam is 1 × 1 μm, and the reflections originate mostly from the sample surface but can extend all the way into the sample for 100 μm (CXRO), with sensitivity decreasing with depth. Clearly the diffraction spots in Fig. 6 are not single spots for the *Pinctada* species as they are for Haliotis. In *Pf* and *Pm* each diffraction spot is elongated into a smear, and all smears have very similar shapes. This demonstrates that, within the 100-μm beam path, the calcite crystal is not perfectly co-oriented, but slightly and gradually tilting in orientation. The spread in position of each reflection provides a measurement of the angle spread within one crystalline domain. Hence a crystalline domain is defined as a region of space in which all crystals can be indexed as a co-oriented, or nearly co-oriented, single crystal of calcite, generating a diffraction pattern of spots, or smears, respectively. A crystalline domain may be a prism (e.g. in *Haliotis* or *Atrina* species), or a sub-prismatic domain as observed by PIC-mapping in Fig. 5 for *Pf* and *Pm*. Adjacent crystalline domains are separated by abrupt color changes in Figs. 2 and 4.

Notice that the color gradient observed in *Pf* and *Pm* in Fig. 4 within each crystalline domain shows a gradual tilt in crystal lattice orientation as one moves from pixel to pixel in the *XY* plane of the image. The smear of each reflection in *Pf* and *Pm* in Fig. 6, instead, reveals an angle spread along the *Z*-direction, that is, the depth direction into the sample surface. Whether the latter is a gradual tilt or a cluster of particles abruptly changing orientation from particle to particle one cannot say from Fig. 6 alone. Because a gradual tilt is evident in the color maps of Fig. 4 for several domains, however, we can safely conclude that the crystal lattice orientation changes by gradually tilting in 3-dimensional space. Such tilt must be taking place within each of the sub-prism domains that appear co-oriented in Fig. 5. Using PIC-mapping we have observed a small number, between 1 and 6, of these domains in each prism of *Pf* and *Pm* shells.

Finally, to ascertain if any of the structural parameters observed in all shell species affect the materials properties of the prisms, we did microindentation experiments. Specifically, we indented the

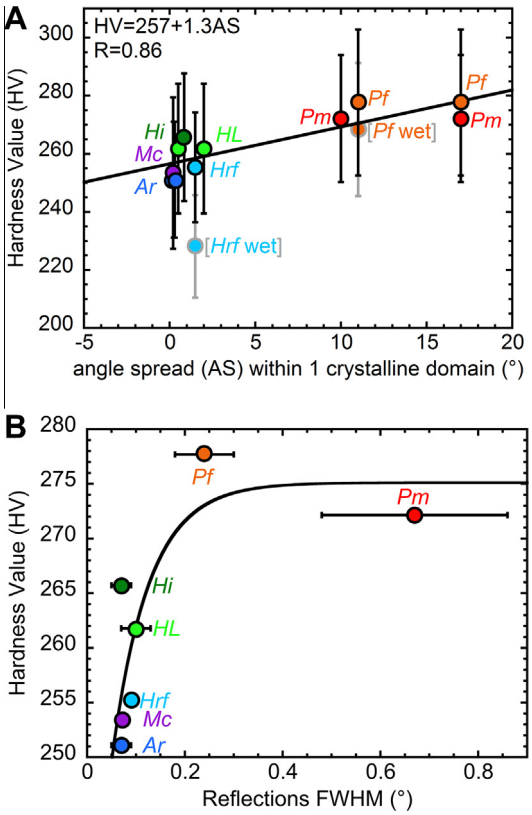

Fig.7. (A) Correlation of the hardness values (HV) and angle spread (AS) measured in all the species with a calcite prismatic layer. The HV was measured by microindentation and the AS by microdiffraction, as shown in Figs. 2, 4 and 6. The data for *Hrf* wet and *Pf* wet samples, soaked in seawater for 24 h before microindentation analysis, are shown for comparison here but were not included in the linear fit. The HV was calculated based on the length of the indent diagonals, as measured with SEM imaging, and the error bars on HV are the standard deviation of all measurements, as shown in Table 1. AS is a maximum spread, that is, the aperture of the cone in which all angles are contained, hence it has no error bars. Clearly the *Pinctada* species prisms are harder than any other calcite prisms analyzed. This correlation, with $R = 0.86$ and $R^2 = 0.74$, is very strong. A correlation coefficient R greater than 0.4 is generally accepted as proof of correlation. Given the strength of this correlation, we hypothesize that the newly discovered orientation gradient within each crystalline domain may increase the hardness of the prismatic layer in the *Pinctada* species. The strong correlation observed here also applies to the hardness values measured with VLM imaging, with the best-fit line HV = 258 + 1.8 AS and correlation coefficient $R = 0.88$ and $R^2 = 0.77$. (B) The hardness values (HV) also correlate with the reflection width: the greater the full width at half maximum (FWHM) of the reflections the greater the hardness. The FWHM shown is the average of 10 measurements for each species. The horizontal error bars are the standard deviations across these 10 measurements (Table 2). The vertical error bars are omitted for clarity, and are identical to those in A. The reflection width, expressed here as FWHM, is an indirect measure of nanoparticle size, hence this plot is conceptually similar to a Hall–Petch plot (Hall, 1951; Meyers et al., 2006; Petch, 1953). For *Pm* the nanoparticle size is estimated to be on the order of 20 nm, for all other species the size is greater.

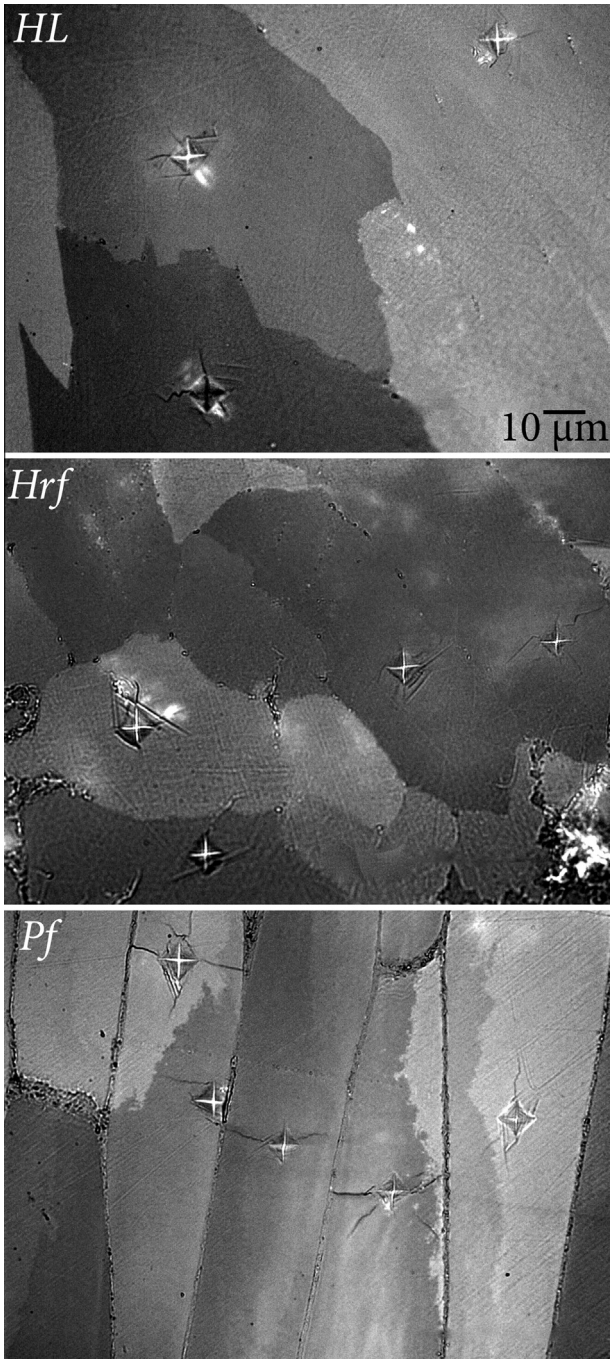

Fig.8. Visible light micrographs of three microindented shell samples from *HL*, *Hrf*, *Pf*. The images are obtained with crossed-polarizers, hence different gray levels indicate different calcite crystal orientations. The tip of the indenter leaves a larger pyramidal dent in softer materials than in harder materials. All micrographs share the same 10-µm scale bar.

center of individual prisms in all shells, and measured the hardness. In Table 1 we present the microindentation results, which show that *Np* has the hardest prisms, as expected, since aragonite is harder than calcite (Table 1). Among the prismatic calcite shells, the results clearly show much greater hardness for the *Pinctada* species than for other shells. With $p \leqslant 0.05$ (down to 3×10^{-6}), the data indicate with a confidence level of 95% or better that the *Pf* and *Pm* prisms are harder than all other calcite prisms analyzed.

Most interestingly, for all prismatic calcite shells, we find a strong correlation ($R = 0.86$) between the hardness value and the angle spread within each crystalline domain, as shown in Fig. 7A. The hardness value also correlates with the reflection width, as shown in Fig. 7B. The data for this plot are presented in Table 2. Fig. 8 shows the pyramidal microindents in shells from three different species. The angle spread HV data in Fig. 7 were obtained from these and many more indents, as shown in Table 1.

4. Discussion

The size, crystal orientation, and arrangement of prisms in all shells analyzed, except for the *Pinctada* species, confirmed previous observations (Berman et al., 1993; Blank et al., 2003; Bøggild, 1930; Carter, 1990; Checa et al., 2005; Dauphin, 2003; Dodd, 1964, 1966; Gilbert et al., 2011; Gray and Smith, 2004; Mutvei, 1964, 1989; Nakahara and Bevelander, 1971; Nudelman et al., 2007; Suzuki and Uozumi, 1981; Taylor and Layman, 1972; Tsujii et al., 1958; Watabe and Wada, 1956; Weiner, 1983). However, we found four unprecedented, surprising, and potentially important results, all of them involving the *Pinctada* species:

1. Prisms in *Pf* and *Pm* are significantly harder than calcitic prisms in the other shells analyzed. Using VLM micrographs to measure indent diagonals, *Pf* and *Pm* are significantly harder than all others, with *p*-values 0.000003–0.05. Using SEM micrographs gives a similar result, with *p*-values 0.000004–0.05 for all shells, except for a *p*-value of 0.1 for *Pm* vs *Hi*, suggesting that the hardness of *Pm* and *Hi* is not significantly different at the 95% confidence level.
2. Crystalline domains within each prism in *Pf* and *Pm* are not co-oriented single crystals but have an angle spread between 10° and 20°.
3. Increased hardness is strongly correlated with the angle spread within each crystalline domain, and both are highest in *Pf* and *Pm*.
4. Increased hardness is correlated with reflection width, which is highest in *Pf* and *Pm*.

Based on these four observations, one can hypothesize that the orientation gradient within each crystalline domain, reported here for the first time, is the structural property that confers increased hardness to the prisms of the *Pinctada* species. As greater hardness signifies greater resistance to wear (Khruschov, 1974), the increased hardness of the prismatic layer may be an advantage for these organisms in their environment. We speculate that the materials property of increased resistance to wear may also provide an evolutionary advantage to the *Pinctada* species.

The subdivision of prisms into differently oriented crystalline domains is consistent with previous observations (Dauphin, 2003; Gilbert et al., 2011; Okumura et al., 2010, 2011).

The 10–20° angle spread within each domain in *Pf* and *Pm* in Figs. 4 and 6 reveals a gradually changing crystal orientation in a calcite biomineral. This gradual change takes place in the bulk of the prisms, and is consistent with the observations Okumura et al. made on the surface of calcite prisms (Okumura et al., 2010). The slight, gradual tilting of the crystal lattice appears as a gradient of color in the microdiffraction maps in Fig. 4, and as smeared reflections in Fig. 6. A similar effect was observed in aragonite nacre and interpreted as the result of "bridge-tilting", as nacre grows near-epitaxially (Olson et al., 2013a,b). The gradually rotating bulk orientation shown here is the first reported for a calcite biomineral.

It has been demonstrated that molluscan larvae form their shells via an amorphous precursor phase (Hasse et al., 2000; Neues et al., 2007; Weiss et al., 2002) and it is thought that adult mollusks do so as well (Baronnet et al., 2008; Nudelman et al., 2007; Wolf

et al., 2012). In principle the observation that crystal lattices tilt in prisms could be central to determining how prisms are formed: (i) via amorphous calcium carbonate (ACC) precursors as suspected by many authors (Baronnet et al., 2008; Dauphin, 2008; Jacob et al., 2011; Nudelman et al., 2007) or (ii) via oriented attachment (Penn and Banfield, 1998a,b). It is possible that (i) prisms form by crystallinity propagating (Killian et al., 2009) centripetally (Wolf et al., 2012) through a fully aggregated, space-filling (Yang et al., 2011), anhydrous (Gong et al., 2012), amorphous calcium carbonate precursor. This precursor in prisms may be a polymer-induced liquid precursor (PILP) (Gower and Odom, 2000; Wolf et al., 2012). Alternatively, (ii) it is possible that prisms form by oriented attachment (Penn and Banfield, 1998a,b) of previously crystallized calcite nanoparticles. Direct evidence of amorphous precursors that later crystallize into calcitic prisms has not been described yet by any authors, thus one must maintain an open mind and also consider the possibility that particles crystallized first, and then aggregated into prisms by oriented attachment. The PIC-maps of Fig. 5 are consistent with either of these two possibilities. It is known that in oriented attachment particles do not have to be perfectly co-oriented, in fact long, thin, pseudo-single crystals formed via oriented attachment can be curved over long distances (Chan et al., 2004). However, also single-crystalline calcite nanorods (100 nm wide, 10 μm long) formed via an amorphous calcium carbonate precursor (Kim et al., 2011a) were recently analyzed for long-range crystal orientation, and found to show gradually tilting lattices (Fiona Meldrum, personal communication). Both possibilities, (i) amorphous nanoparticle aggregation, then crystallization or (ii) nanoparticle crystallization, then aggregation, are therefore consistent with the lattice tilting described here, hence this observation is not useful to discriminate between formation mechanisms.

Another aspect apparent in the *Pinctada* species in Fig. 5 is that their prisms are clearly subdivided into 50–100 nm nanoparticles. This is observed as the size of the irregularities at the boundary between adjacent crystalline domains with different orientations, displayed in Fig. 5 as different gray levels. This nanoparticle size is in agreement with previous observations (Bruet et al., 2005; Dauphin, 2001, 2008; Gilbert et al., 2011; Li et al., 2004; Okumura et al., 2010, 2011; Wolf et al., 2012). Could it be this subdivision into nanoparticles that makes *Pinctada* prisms harder? The Fratzl group showed that subdivision into nanocrystals confers robustness, that is, resistance to flaws to biominerals (Fratzl and Weinkamer, 2007; Gao et al., 2003). Wolf et al. (2012) observed nanoparticles in *Pinna nobilis*, a shell similar to *Atrina rigida*, and other authors found nanoparticles in prisms of a variety of shells (Suzuki and Uozumi, 1981; Taylor and Layman, 1972; Tsujii et al., 1958). Zooming into Fig. 5 (see images provided online as a tif file) one can see irregularities of the same 50–100 nm size at orientation boundaries in *Np*, *Pf*, *Pm*, and with >200 nm sizes in *Hrf*, *HL* and *Mc*. It is therefore reasonable to assume that most if not all shells form their prisms starting from nanoparticles, and that the subdivision of *Pf* and *Pm* prisms into smaller nanocrystals may also be the source of increased hardness. The plot in Fig. 7B shows a clear correlation between hardness and reflection width. We note that the reflection width is, as a first approximation, inversely proportional to the nanoparticle size, in fact the smaller the nanoparticles the greater the width of their reflections. However, the smallest particles of *Pf* and *Pm* also exhibit the greatest angle spread within a single domain, hence a causal relationship between nanoparticle size, angle spread, and hardness cannot be established with the available data. Further experiments are necessary to accurately and directly measure nanoparticle sizes and correlate those with their angle spreads: atomic force microscopy (AFM) and electron back-scatter diffraction (EBSD) are probably better suited methods to obtain these measurements, and to provide quantitative relationships between these structural parameters.

The lattice tilting described here in calcite prisms is a very simple strategy to obtain crystalline angle spreads. It is therefore possible that greater angle spread provides the crystalline prisms with greater hardness, and in turn hardness provides resistance to wear.

5. Conclusions

We have shown that the prismatic layers in shells from different species are structurally different. Most remarkably, the calcite prisms of the *Pinctada* species are subdivided into sub-prismatic domains of orientations, and within each of these domains the calcite crystal lattice tilts gradually over long distances, on the order of 10–100 μm. Prisms from the *Pinctada* species are harder than any other calcite prisms analyzed, and this is not by coincidence: there is a strong correlation between the angle spread of crystal orientations and the hardness of the prismatic crystals, suggesting a structure–property relationship. If confirmed by further experimental evidence, this could be the first structure–property relationship in mollusk shell prisms.

Online materials Tables 1 and 2 are provided as Excel files, so the readers can use the numbers to the accuracy they prefer. High-resolution versions of Figs. 1, 3 and 5 are provided as tif files, so the reader can zoom in and out at will.

Note added in proof

As this manuscript went to press we noticed the preprint of another article finding results in prefect agreement with those presented here for the angle spread in *Pm* prisms (Checa et al., 2013).

Acknowledgments

We are grateful to an anonymous reviewer for requiring the Hall–Petch plot in Fig. 7B. We thank Robert O. Ritchie for discussions. We thank ALS beamline scientists Andreas Scholl and Anthony Young for their technical support during the PEEM-3 experiments, and Richard Celestre for help during shell sample preparation. This work was supported by NSF award DMR-1105167, and DOE Award DE-FG02-07ER15899 to PUPAG, and by NSF award EAR-103979 to RAM. The experiments were performed at the Berkeley Advanced Light Source, supported by DOE under contract DE-AC02-05CH11231.

Appendix A. Supplementary data

Supplementary data associated with this article can be found, in the online version, at http://dx.doi.org/10.1016/j.jsb.2013.06.006.

References

Aizenberg, J., Albeck, S., Weiner, S., Addadi, L., 1994. Crystal–protein interactions studied by overgrowth of calcite on biogenic skeletal elements. J. Cryst. Growth 142, 156–164.

Baronnet, A., Cuif, J.P., Dauphin, Y., Farre, B., Nouet, J., 2008. Crystallization of biogenic Ca-carbonate within organo-mineral micro-domains. Structure of the calcite prisms of the Pelecypod *Pinctada margaritifera* (mollusca) at the submicron to nanometre ranges. Mineral. Mag. 72, 617–626.

Berman, A., Hanson, J., Leiserowitz, L., Koetzle, T.F., Weiner, S., et al., 1993. Biological control of crystal texture: a widespread strategy for adapting crystal properties to function. Science 259, 776–779.

Blank, S., Arnoldi, M., Khoshnavaz, S., Treccani, L., Kuntz, M., et al., 2003. The nacre protein perlucin nucleates growth of calcium carbonate crystals. J. Microsc. 212, 280–291.

Bøggild, O.B., 1930. The shell structure of the mollusks. Kongl. Danske Vidensk. Selsk. Skrifter, Naturv.-Math. Afd. 2, 231–326.

Bruet, B.J.F., Qi, H.J., Boyce, M.C., Panas, R., Tai, K., et al., 2005. Nanoscale morphology and indentation of individual nacre tablets from the gastropod mollusc Trochus niloticus. J. Mater. Res. 20, 2400–2419.

Carpenter, W.B., 1844. On the microscopic structure of shells. Rep. Brit. Ass. Adv. Sci. 14, 1–24.

Carter, J.G., 1980. Guide to bivalve shell microstructures. In: Rhoads, D.C., Lutz, R.A. (Eds.), Skeletal Growth of Aquatic Organisms. Plenum, New York, NY.

Carter, J.G., 1990. Skeletal Biomineralization: Patterns, Processes and Evolutionary Trends. Van Nostrand Reinhold, New York, NY.

Chan, C.S., De stasio, G., et al., 2004. Microbial polysaccharides template assembly of nanocrystal fibers. Science 303, 1656–1658.

Checa, A.G., Rodriguez-Navarro, A.B., Esteban-Delgado, F.J., 2005. The nature and formation of calcitic columnar prismatic shell layers in pteriomorphian bivalves. Biomaterials 26, 6404–6414.

Checa, A.G., Esteban-Delgado, F.J., Ramirez-Rico, J., Rodriguez-Navarro, A.B., 2009. Crystallographic reorganization of the calcitic prismatic layer of oysters. J. Struct. Biol. 167, 261–270.

Checa, A.G., Bonarski, J.T., Willinger, M.G., Faryna, M., Berent, K., et al., 2013. Crystallographic orientation inhomogeneity and crystal splitting in biogenic calcite. J. R. Soc. Interface 10, in press, http://dx.doi.org/10.1098/rsif.2013.0425.

CXRO, 2013. Center for X-Ray Optics, X-ray attenuation length calculator: http://henke.lbl.gov/optical_constants/atten2.html.

Dauphin, Y., 2001. Nanostructures de la nacre des tests de céphalopodes actuels. Palaeont. Z. 75, 113–122.

Dauphin, Y., 2003. Soluble organic matrices of the calcitic prismatic shell layers of two pteriomorphid bivaleves, *Pinna nobilis* and *Pinctada margaritifera*. J. Biol. Chem. 278, 15168–15177.

Dauphin, Y., 2008. The nanostructural unity of mollusc shells. Mineral. Mag. 72, 243–246.

De Stasio, G., Koranda, S.F., Tonner, B.P., Harp, G.R., Mercanti, D., et al., 1992a. X-Ray Secondary-Emission Microscopy (XSEM) of neurons. Europhys. lett. 19, 655–659.

De Stasio, G., Perfetti, P., Oddo, N., Galli, P., Mercanti, D., et al., 1992b. Metal uptake in neuron cultures - a systematic study. NeuroReport 3, 965–968.

De Stasio, G., Hardcastle, S., Koranda, S.F., Tonner, B.P., Mercanti, D., et al., 1993a. Photoemission spectromicroscopy of neurons. Phys. Rev. E 47, 2117–2121.

De Stasio, G., Dunham, D., Tonner, B.P., Mercanti, D., Ciotti, M.T., et al., 1993b. Aluminum in rat cerebellar neural cultures. NeuroReport 4, 1175–1178.

De Stasio, G., Frazer, B.H., Gilbert, B., Richter, K.L., Valley, J.W., 2003. Compensation of charging in X-PEEM: a successful test on mineral inclusions in 4.4 Ga old zircon. Ultramicroscopy 98, 57–62.

Dodd, J.R., 1964. Environmentally controlled variation in the shell structure of a pelecypod species. J. Paleontol. 38, 1065–1071.

Dodd, J.R., 1966. Diagenetic stability of temperature-sensitive skeletal properties in *Mytilus* from the Pleistocene of California. Geol. Soc. Am. Bull. 77, 1213–1224.

Fratzl, P., Weinkamer, R., 2007. Nature's hierarchical materials. Prog. Mater Sci. 52, 1263–1334.

Frazer, B.H., Gilbert, B., Sonderegger, B.R., De Stasio, G., 2003. The probing depth of total electron yield in the sub keV range: TEY-XAS and X-PEEM. Surf. Sci. 537, 161–167.

Gao, H., Ji, B., Jäger, I.L., Arzt, E., Fratzl, P., 2003. Materials become insensitive to flaws at nanoscale: lessons from nature. Proc. Natl. Acad. Sci. USA 100, 5597–5600.

Gilbert, P.U.P.A., 2012. Polarization-dependent Imaging Contrast (PIC) mapping reveals nanocrystal orientation patterns in carbonate biominerals. In: Kiskinova, M., Scholl, A. (Eds.), J. Electron Spectrosc. Relat. Phenom. Special Issue on Photoelectron Microscopy. Time-Resolved Pump-Probe PES. Elsevier, pp. 395–405.

Gilbert, B., Frazer, B.H., Naab, F., Fournelle, J., Valley, J.W., et al., 2003. X-ray absorption spectroscopy of silicates for in situ, sub-micrometer mineral identification. Am. Mineral 88, 763–769.

Gilbert, P.U.P.A., Frazer, B.H., Abrecht, M., 2005. The organic-mineral interface in biominerals. In: Banfield, J.F. et al. (Eds.), Molecular Geomicrobiology Reviews in Mineralogy and Geochemistry. Mineralogical Society of America, Washington DC, p. 1570185.

Gilbert, P.U.P.A., Metzler, R.A., Zhou, D., Scholl, A., Doran, A., et al., 2008. Gradual ordering in red abalone nacre. J. Am. Chem. Soc. 130, 17519–17527.

Gilbert, P.U.P.A., Young, A., Coppersmith, S.N., 2011. Measurement of *c*-axis angular orientation in calcite (CaCO3) nanocrystals using x-ray absorption spectroscopy. Proc. Natl. Acad. Sci. USA 108, 11350–11355.

Gong, Y.U.T., Killian, C.E., Olson, I.C., Appathurai, N.P., Amasino, A.L., et al., 2012. Phase transitions in biogenic amorphous calcium carbonate. Proc. Natl. Acad. Sci. USA 109, 6088–6093.

Gotliv, B.A., Kessler, N., Sumerel, J.L., Morse, D.E., Tuross, N., et al., 2005. Asprich: a novel aspartic acid-rich protein family from the prismatic shell matrix of the bivalve *Atrina rigida*. ChemBioChem 6, 304–314.

Gower, L.B., Odom, D.J., 2000. Deposition of calcium carbonate films by a polymer-induced liquid-precursor (PILP) process. J. Cryst. Growth 210, 719–734.

Gray, B.E., Smith, A.M., 2004. Mineralogical variation in shells of the blackfoot abalone, *Haliotis iris* (Mollusca: Gastropoda: Haliotidae), in southern New Zealand. Pac. Sci. 58, 47–64.

Hall, E.O., 1951. The deformation and ageing of mild steel: III discussion of results. Proc. Phys. Soc., Sect. B 64, 747.

Hasse, B., Ehrenberg, H., Marxen, J.C., Becker, W., Epple, M., 2000. Calcium carbonate modifications in the mineralized shell of the freshwater snail Biomphalaria glabrata. Chem. Eur. J. 6, 3679–3685.

Jacob, D.E., Wirth, R., Soldati, A.L., Wehrmeister, U., Schreiber, A., 2011. Amorphous calcium carbonate in the shells of adult Unionoida. J. Struct. Biol. 173, 241–249.

Kearney, C., Zhao, Z., Bruet, B.J.F., Radovitzky, R., Boyce, M.C., et al., 2006. Nanoscale anisotropic plastic deformation in single crystal aragonite. Phys. Rev. Lett. 96, 255505.

Khruschov, M.M., 1974. Principles of abrasive wear. Wear 28, 69–88.

Killian, C.E., Metzler, R.A., Gong, Y.U.T., Olson, I.C., Aizenberg, J., et al., 2009. Mechanism of calcite co-orientation in the sea urchin tooth. J. Am. Chem. Soc. 131, 18404–18409.

Killian, C.E., Metzler, R.A., Gong, Y.U.T., Churchill, T.H., Olson, I.C., et al., 2011. Self-sharpening mechanism of the sea urchin tooth. Adv. Funct. Mater. 21, 682–690.

Kim, Y.Y., Hetherington, N.B.J., Noel, E.H., Kroger, R., Charnock, J.M., et al., 2011a. Capillarity creates single-crystal calcite nanowires from amorphous calcium carbonate. Angew. Chem., Int. Ed. 50, 12572–12577.

Kim, Y.Y., Ganesan, K., Yang, P.C., Kulak, A.N., Borukhin, S., et al., 2011b. An artificial biomineral formed by incorporation of copolymer micelles in calcite crystals. Nat. Mater. 10, 890–896.

Launey, M.E., Ritchie, R.O., 2009. On the fracture toughness of advanced materials. Adv. Mater. 21, 2103–2110.

Li, X., Chang, W.C., Chao, Y.J., Wang, R., Chang, M., 2004. Nanoscale structural and mechanical characterization of a natural nanocomposite material: the shell of red abalone. Nano Lett. 4, 613–617.

Li, H., Xin, H.L., Kunitake, M.E., Keene, E.C., Muller, D.A., et al., 2011. Calcite prisms from mollusk shells (*Atrina rigida*): swiss-cheese-like organi-inorganic single-crystal composites. Adv. Funct. Mater. 21, 2028–2034.

Lowenstam, H.A., 1954a. Environmental relations of modification compositions of certain carbonate secreting marine invertebrates. Proc. Natl. Acad. Sci. USA 40, 39.

Lowenstam, H.A., 1954b. Factors affecting the aragonite: calcite ratios in carbonate-secreting marine organisms. J. Geol. 62, 284–322.

Lowenstam, H.A., Weiner, S., 1989. On Biomineralization Oxford University Press. Oxford.

Ma, Y., Aichmayer, B., Paris, O., Fratzl, P., Meibom, A., et al., 2009. The grinding tip of the sea urchin tooth exhibits exquisite control over calcite crystal orientation and Mg distribution. Proc. Natl. Acad. Sci. USA 106, 6048–6053.

MacDonald, J., Freer, A., Cusack, M., 2010. Alignment of crystallographic *c*-axis throughout the four distinct microstructural layers of the oyster Crassostrea gigas. Cryst. Growth Des. 10, 1243–1246.

Mann, S., 2001. Biomineralization: Principles and Concepts in Bioinorganic Materials Chemistry. Oxford University Press, New York.

Marie, B., Joubert, C., Tayale, A., Zanella-Cleon, I., Belliard, C., et al., 2012. Different secretory repertoires control the biomineralization processes of prism and nacre deposition of the pearl oyster shell. Proc. Natl. Acad. Sci. USA 109, 20986–20991.

Metzler, R.A., Abrecht, M., Olabisi, R.M., Ariosa, D., Johnson, C.J., et al., 2007. Architecture of columnar nacre, and implications for its formation mechanism. Phys. Rev. Lett. 98, 1–4.

Metzler, R.A., Zhou, D., Abrecht, M., Chiou, J.W., Guo, J.H., et al., 2008a. Polarization-dependent imaging contrast in abalone shells. Phys. Rev. B: Condens. Matter Mater. Phys. 77, 1–9.

Metzler, R.A., Kim, I.W., Delak, K., Evans, J.S., Zhou, D., et al., 2008b. Probing the organic-mineral interface at the molecular level in model biominerals. Langmuir 24, 2680–2687.

Metzler, R.A., Evans, J.S., Killian, C.E., Zhou, D., Churchill, T.H., et al., 2010. Nacre protein fragment templates lamellar aragonite growth. J. Am. Chem. Soc. 132, 6329–6334.

Meyers, M.A., Mishra, A., Benson, D.J., 2006. Mechanical properties of nanocrystalline materials. Prog. Mater Sci. 51, 427–556.

Moureaux, C., Pérez-Huerta, A., Compère, P., Zhu, W., Leloup, T., et al., 2010. Structure, composition and mechanical relations to function in sea urchin spine. J. Struct. Biol. 170, 41–49.

Munch, E., Launey, M.E., Alsem, D.H., Saiz, E., Tomsia, A.P., et al., 2008. Tough, bio-inspired hybrid materials. Science 322, 1516–1520.

Mutvei, H., 1964. On the shells of Nautilus and Spirula: with notes on shell secretion in non-cephalopod molluscs Almqvist & Wiksell.

Mutvei, H., 1989. Structure of molluscan prismatic shell layers. In: Crick, R.E. (Ed.), Origin, Evolution, and Modern Aspects of Biomineralization in Plants and Animals. Plenum Press, New York, pp. 137–151.

Nakahara, H., Bevelander, G., 1971. The formation and growth of the prismatic layer of *Pinctada radiata*. Calcif. Tissue Int. 7, 31–45.

Ndao, M., Keene, E., Amos, F.F., Rewari, G., Ponce, C.B., et al., 2010. Intrinsically disordered mollusk shell prismatic protein that modulates calcium carbonate crystal growth. Biomacromolecules 11, 2539–2544.

Nehrke, G., Nouet, J., 2011. Confocal Raman microscope mapping as a tool to describe different mineral and organic phases at high spatial resolution within marine biogenic carbonates: case study on *Nerita undata* (Gastropoda, Neritopsina). Biogeosciences 8, 3761–3769.

Neues, F., Ziegler, A., Epple, M., 2007. The composition of the mineralized cuticle in marine and terrestrial isopods: a comparative study. CrystEngComm 9, 1245–1251.

Nudelman, F., Chen, H.H., Goldberg, H.A., Weiner, S., Addadi, L., 2007. Lessons from biomineralization: comparing the growth strategies of mollusc shell prismatic and nacreous layers in *Atrina rigida*. Faraday Discuss. 136, 9–25.

Okumura, T., Suzuki, M., Nagasawa, H., Kogure, T., 2010. Characteristics of biogenic calcite in the prismatic layer of a pearl oyster, *Pinctada fucata*. Micron 41, 821–826.

Okumura, T., Suzuki, M., Nagasawa, H., Kogure, T., 2011. Microstructural variation of biogenic calcite with intracrystalline organic macromolecules. Cryst. Growth Des. 12, 224–230.
Olson, I.C., Gilbert, P.U.P.A., 2012. Aragonite crystal orientation in mollusk shell nacre may depend on temperature. The angle spread of crystalline aragonite tablets records the water temperature at which nacre was deposited by *Pinctada margaritifera*. Faraday Discuss. 159, 421–432.
Olson, I.C., Kozdon, R., Valley, J.W., Gilbert, P.U.P.A., 2012. Mollusk shell nacre ultrastructure correlates with environmental temperature and pressure. J. Am. Chem. Soc. 134, 7351–7358.
Olson, I.C., Blonsky, A.Z., Tamura, N., Kunz, M., Gilbert, P.U.P.A., 2013a. Crystal nucleation and near-epitaxial growth in nacre. arXiv:1301.6273 [physics.bio-ph].
Olson, I.C., Blonsky, A.Z., Tamura, N., Kunz, M., Gilbert, P.U.P.A., 2013b. Crystal nucleation and near-epitaxial growth in nacre. submitted.
Penn, R.L., Banfield, J.F., 1998a. Oriented attachment and growth, twinning, polytypism, and formation of metastable phases: insights from nanocrystalline TiO2. Am. Mineral. 83, 1077–1082.
Penn, R.L., Banfield, J.F., 1998b. Imperfect oriented attachment: dislocation generation in defect-free nanocrystals. Science 281, 969–971.
Perez-Huerta, A., Dauphin, Y., Cuif, J.-P., Cusack, M., 2011. High resolution electron backscatter diffraction (EBSD) data from calcite biominerals in recent gastropod shells. Micron 42, 246–251.
Petch, N.J., 1953. The cleavage strength of polycrystals. J. Iron Steel Inst. 174, 25–28.
Politi, Y., Mahamid, J., Goldberg, H., Weiner, S., Addadi, L., 2007. Asprich mollusk shell protein: in vitro experiments aimed at elucidating function in $CaCO_3$ crystallization. CrystEngComm 9, 1171–1177.
Ritchie, R.O., 2011. The conflicts between strength and toughness. Nat. Mater. 10, 817–822.
Rousseau, M., Lopez, E., Stempfle, P., Brendle, M., Franke, L., et al., 2005. Multiscale structure of sheet nacre. Biomaterials 26, 6254–6262.
Schmahl, W.W., Griesshaber, E., Merkel, C., Kelm, K., Deuschle, J., et al., 2008. Hierarchical fibre composite structure and micromechanical properties of phosphatic and calcitic brachiopod shell biomaterials, an overview. Mineral. Mag. 72, 541–562.
Suzuki, S., Uozumi, S., 1981. Organic components of prismatic layers in molluscan shells. J. Fac. Sci. Hokkaido Univ. Ser. IV 20, 7–20.
Tamura, N., MacDowell, A.A., Spolenak, R., Valek, B.C., Bravman, J.C., et al., 2003. Scanning X-ray microdiffraction with submicrometer white beam for strain/stress and orientation mapping in thin films. J. Synchrotron Radiat. 10, 137–143.
Taylor, J.D., Layman, M., 1972. The mechanical properties of bivalve, (mollusca) shell structures. Paleontology 15, 73–87.
Tsujii, T., Sharp, D.G., Wilbur, K.M., 1958. Studies on shell formation VII. The submicroscopic structure of the shell of the oyster *Crassostrea virginica*. J. Biophys. Biochem. Cy. 4, 275–280.
Wang, R.Z., Addadi, L., Weiner, S., 1997. Design strategies of sea urchin teeth: structure, composition and micromechanical relations to function. Philos. T. R. Soc. B 352, 469.
Watabe, N., Wada, K., 1956. On the shell structures of Japanese pearl oyster *Pinctada martensii* (Dunker). Prismatic Layer. I. Rept. Fac. Fish. Prefict. Univ. Mie. 2, 227–232.
Weiner, S., 1983. Mollusk shell formation: isolation of two organic matrix proteins associated with calcite deposition in the bivalve *Mytilus californianus*. Biochemistry 22, 4139–4145.
Weiss, I.M., Tuross, N., Addadi, L., Weiner, S., 2002. Mollusc larval shell formation: amorphous calcium carbonate is a precursor phase for aragonite. J. Exp. Zool. 293, 478–491.
Wolf, S.E., Lieberwirth, I., Natalio, F., Bardeau, J.F., Delorme, N., et al., 2012. Merging models of biomineralisation with concepts of nonclassical crystallisation: is a liquid amorphous precursor involved in the formation of the prismatic layer of the Mediterranean Fan Mussel Pinna nobilis? Faraday Discuss. 159, 433–448.
Yang, L., Killian, C.E., Kunz, M., Tamura, N., Gilbert, P.U.P.A., 2011. Biomineral nanoparticles are space-filling. Nanoscale 3, 603–609.
Zhang, G.F., Fang, X.D., Guo, X.M., Li, L., Luo, R.B., et al., 2012. The oyster genome reveals stress adaptation and complexity of shell formation. Nature 490, 49–54.